RSC Advances

ROYAL SOCIETY OF CHEMISTRY

PAPER

View Article Online
View Journal | View Issue

Cite this: *RSC Adv.*, 2026, **16**, 9530

From structure to function: a one-dimensional palladium(II) hybrid for real-sample hydroquinone detection

Sarra Bougossa,[a] Naoufel Ben Hamadi,[b] Jassem Wannassi,[c] Noureddine Mhadhbi,[ad] Jeanneau Erwann,[e] Ahlem Guesmi,[b] Lotfi Khezami,[b] Houcine Barhoumi[c] and Houcine Naïli*[a]

A novel one-dimensional (1D) organic–inorganic hybrid compound, $(C_4H_7N_2)[PdCl_3(H_2O)]$, was synthesized through the reaction of palladium(II) chloride with 2-methylimidazole in an aqueous acidic medium. The structure was elucidated through single-crystal X-ray diffraction studies and consists of infinite chains of $[PdCl_3(H_2O)]$ units connected *via* edge-sharing octahedra, stabilized by extensive hydrogen bonding and $\pi\cdots\pi$ stacking interactions involving the organic cations. Infrared spectroscopy confirmed the presence of key functional groups and intermolecular interactions. UV-vis diffuse reflectance spectroscopy indicated significant absorption in the UV range, with an optical band gap of 2.18 eV, indicating semiconducting behavior. The material's structural characteristics and optical behavior suggest its suitability for applications in photocatalysis, sensing, and proton conduction. An electrochemical sensor exhibiting high sensitivity and selectivity for hydroquinone (HQ) detection was developed and tested using differential pulse voltammetry. This sensor demonstrated a low detection limit of 0.02 μM and exhibited a broad linear response range spanning 0.02 to 10 μM. It maintained outstanding performance even when common interfering substances were present. Application to real samples provided recovery rates between 95.4% and 102.4%, underscoring its potential for use in environmental surveillance and quality control purposes.

Received 8th November 2025
Accepted 10th February 2026

DOI: 10.1039/d5ra08631k

rsc.li/rsc-advances

1 Introduction

Dangerous side effects from the use of skin lightening products aimed at erasing freckles and whitening the skin are a major problem that needs to be addressed immediately.[1] The hydroquinone in these products suppresses melanin production in the skin and whitens the skin.[2] The European Union (EU) and the Environmental Protection Agency (EPA) have banned hydroquinone from cosmetics because long-term use causes many side effects.[3] However, hydroquinone is still used illegally in skin-whitening cosmetics in developing countries.[4] In the United States, the Food and Drug Administration suggests a concentration of skin lightening agents of 1.5 to 2%.[5] In some countries, skin whitening products may contain higher concentrations. Heavy metal allergies can cause health problems such as allergic contact dermatitis.[6] Metal allergens are most commonly associated with nickel (Ni), chromium (Cr), cobalt (Co) and copper (Cu).[7] Nickel-induced dermatitis is most commonly caused by exposure to nickel, with levels decreasing to 0.5 to 1.0 ppm on repeated exposure or on separate occasions.[8] Depending on the duration of exposure and individual sensitivity, hexavalent chromium can cause dermatitis at concentrations ranging from 1 mg kg^{-1} to 20 mg (ppb).[9] Dermatologists have reported adverse effects of cobalt and copper, typically occurring at concentrations in the ppm range due to occupational exposure.[10] Evidence shows that monitoring very low levels of trace metal ions can reduce potential health risks.[11]

While HQ can be effective as a skin-lightening agent when applied correctly, it is also associated with potential adverse effects, including skin irritation, increased photosensitivity, and paradoxical pigmentation.[12] To enhance its depigmenting efficacy, HQ is often formulated in combination with alpha hydroxy acids (AHAs), which act as exfoliating agents to accelerate the removal of pigmented keratinocytes.[13] Hydroquinone undergoes a reversible redox transformation to benzoquinone through a two-electron and two-proton process.[14] This

---

[a] *Laboratory Physical-Chemistry of the Solid State, Department of Chemistry, Faculty of Sciences of Sfax, BP 1171, Sfax 3000, University of Sfax, , Tunisia. E-mail: houcine_naili@yahoo.com*

[b] *Chemistry Department, College of Science, Imam Mohammad Ibn Saud Islamic University (IMSIU), P.O. Box 5701, Riyadh 11432, Saudi Arabia*

[c] *Laboratory of Interfaces and Advanced Materials, Faculty of Sciences, University of Monastir, 5019 Monastir, Tunisia*

[d] *University of Monastir, Preparatory Institute for Engineering Studies of Monastir, 5019 Monastir, Tunisia*

[e] *Centre de Diffractométrie Henri Longchambon, Université Claude Bernard Lyon1, 5 rue de La Doua, 69100 Villeurbanne, France*

conversion occurs *via* electrochemical oxidation, as described by the following reaction: $HQ \rightleftharpoons BQ + 2H^+ + 2e^-$.[15] Under electrochemical measurements, this process usually occurs under mild circumstances in aqueous mediums without the need of chemical oxidants.[16] Since the reaction is very reversible, it is impossible to determine an isolated chemical yield. Instead, electrochemical characteristics including peak current, peak potential separation and reversibility which serve as the foundation for electrochemical sensing applications are used to assess the effectiveness of the HQ/BQ redox process.[17]

The determination of hydroquinone (HQ) has been achieved through a combination of chromatographic[18] and spectrophotometric methods,[19] among other analytical techniques. High-selectivity is a characteristic of certain chromatographic techniques, such as HPLC, LC-MS and GC, which typically have LODs that range from 0.01 to 0.5 M, depending on the sample matrix and detector.[20] The use of spectrometry techniques such as UV-vis, colorimetric assays and derivative spectra has enabled the analysis of high-intensity differential coverage (LDP) values within the range of 0.5–010 M for HQ analysis.[21] Other methods also offer similar results.[22] Nevertheless, these methods are often too expensive, require extensive sample preparation and result in lengthy analysis times.[23] Due to these constraints, electrochemical sensors have emerged as straightforward yet highly sensitive substitutes for HQ detection.[24] However, their practical deployment is often hindered by significant drawbacks, including high operational costs, the need for complex and sophisticated instrumentation, time-consuming sample preparation steps, and the instability of biological reagents, all of which can compromise reproducibility and limit shelf life.[25,26] Hybrid electrochemical-optical sensing platforms have gained increasing attention due to their ability to provide complementary analytical information.[27] Dual-mode sensors enable accurate quantitative electrochemical detection while offering optical signals, such as absorbance or fluorescence changes, for visual confirmation and enhanced selectivity.[28] In this context, coupling electrochemical transduction with an optical readout linked to the redox conversion of hydroquinone to benzoquinone could further improve analytical reliability.[29] Although the present study focuses on electrochemical detection, the proposed sensor architecture represents a promising platform for future development of electrochemical-optical dual-mode sensors.[30] To address these limitations, there has been growing interest in developing alternative analytical strategies that combine robustness, cost-effectiveness and ease of integration into portable and user-friendly diagnostic platforms.[31] Among these emerging approaches, electrochemical sensing has garnered particular attention due to its inherent advantages, including operational simplicity, rapid responses, low cost, straightforward sample preparation, and suitability for integration into compact, disposable devices.[32,33] Electrochemical techniques enable real-time, *in situ* monitoring of analytes like HQ with excellent sensitivity and selectivity.[34] Crucially, the analytical performance of electrochemical sensors, including their detection limits, linear dynamic range, selectivity in complex matrices and operational stability, is strongly influenced by the physicochemical properties and electrocatalytic behavior of the materials employed at the electrode interface.[35] Desirable physicochemical properties include high surface area, good electrical conductivity, chemical stability, appropriate porosity and strong electrocatalytic activity, which together enhance electron transfer and overall sensor performance.[36]

In recent years, considerable attention has been devoted to designing nanostructured materials such as MOFs, metallic nanoparticles, conductive polymers and hybrid nanocomposites to boost the catalytic efficiency, sensitivity and functionality of electrochemical sensing devices.[37,38] Recently, organic–inorganic metal halide-based perovskites have garnered attention due to their promising properties for optoelectronic, catalytic and sensing applications.[39–41] Although this study focuses on electrochemical sensing, the structural features of organic–inorganic hybrids,[42] including tunable porosity and potential proton conduction pathways, indicate that these materials may also be explored as proton-conducting components in fuel cells, representing a potential avenue for future applications.[43] These compounds uniquely combine the synthetic flexibility of organic molecules with the stability and coordination versatility of inorganic metal centers.[44] This combination of properties has led to the design of these materials, shaped by the metal centers' coordination geometry and the organic linkers, thus enhancing their potential in various technological applications.[45] The dimensionality of organic–inorganic hybrid (OIH) materials plays a pivotal role in defining their physical and chemical behaviors.[46] Among them, one-dimensional (1D) architectures have garnered significant attention due to their anisotropic properties, enhanced surface area, and potential for directional charge or energy transport.[47] The tunability afforded by coordination chemistry enables precise control over their composition and functionality, facilitating the design of materials with tailored properties.[48] As a result, 1D hybrid materials have found promising applications in diverse fields, including optoelectronics,[49] biological and biomedical applications,[50] energy storage and conversion,[51] photocatalysis for environmental remediation[52] and sensing technologies.[53] One-dimensional (1D) architectures, including nanowires, nanorods, and nanotubes, have attracted increasing attention due to their high surface-to-volume ratios and favorable energy/charge transport properties.[54] Depending on the material composition and structural design, such 1D nanostructures typically exhibit specific surface areas ranging from tens to several hundreds of $m^2\ g^{-1}$, particularly in porous or hierarchical configurations, providing a large number of accessible active sites.[55] Moreover, their anisotropic geometry offers continuous and directional pathways for charge carriers, leading to enhanced electron mobility, reduced grain boundary resistance, and suppressed charge recombination.[56] These characteristics make 1D architectures especially attractive for electrochemical sensing and energy-related applications.[57] In addition to their applications in materials science, palladium–imidazole complexes have shown significant potential in biological fields, exhibiting antibacterial, anti-cancer and anti-inflammatory properties.[58] The imidazole ring system is well known for its pharmacological importance, owing to its ability to enhance bioavailability and mediate interactions with key biomolecular targets, such as DNA and enzymes.[59] Notably, derivatives of 2-methylimidazoles have shown the ability to disrupt microbial cell membranes and impact enzyme function, making them intriguing scaffolds for therapeutic innovation.[60] In parallel, palladium(II) complexes exhibit cytotoxic profiles comparable to those of platinum-based chemotherapeutics, but operate through distinct molecular mechanisms, offering valuable prospects for the development of next-generation metallopharmaceutical agents with improved selectivity and reduced side effects.[61,62] We herein present the synthesis and in-depth structural study of a novel 1D organic–inorganic hybrid coordination material $(C_4H_7N_2)[PdCl_3(H_2O)]$, formed by the self-assembly of palladium(II) ions and 2-methylimidazole ligands in the presence of water. In the resulting structure, the Pd(II) center exhibits an octahedral coordination geometry, with adjacent Pd-centered units interconnected through bridging interactions to generate one-dimensional inorganic chains. Coordinated water plays a crucial structural role by completing the Pd(II) coordination sphere and stabilizing the extended framework through hydrogen-bonding interactions with the organic cations. The successfully synthesized compound, hereafter referred to as IMPdCl, consists of infinite chains of edge-sharing octahedra. In parallel, palladium(II) complexes exhibit cytotoxic profiles comparable to those of platinum-based chemotherapeutics, but operate through distinct molecular mechanisms. While platinum-based complexes predominantly act through strong and kinetically inert coordination to DNA, resulting in DNA cross-linking and replication inhibition, palladium(II) complexes typically display faster ligand exchange kinetics, enabling more dynamic interactions with proteins, enzymes, and cellular membranes.[63–65]

A comprehensive investigation of the material's properties was conducted through spectroscopic analysis, thermal stability assessment, and UV-vis optical studies, offering valuable insights into its structural and functional behavior. The crystal structure is layered and reinforced by non-covalent interactions such as hydrogen bonds and π–π interactions between the organic components, contributing to its stability.[66] The geometry of the metal coordination, along with these non-covalent interactions, also influences the overall structure and arrangement of the network.[67]

Additionally, a comprehensive investigation of the material's properties was conducted through spectroscopic analysis, thermal stability assessment and UV-vis optical studies, offering valuable insights into its structural and functional behavior. A novel one-dimensional (1D) organic–inorganic hybrid compound, $(C_4H_7N_2)[PdCl_3(H_2O)]$, with well-defined structural motifs and semiconducting properties, was designed and exploited to develop a highly efficient electrochemical sensor for hydroquinone (HQ). The sensor exhibited remarkable sensitivity, excellent selectivity, and a low detection limit of 0.02 μM across a wide linear range of 0.02–10 μM, while maintaining stable and reliable performance even in the presence of common interfering species. As summarized in Table 1, the present sensor outperforms previously reported HQ sensors in terms of detection limit, linear range, and selectivity, highlighting the advantages of the hybrid material. These findings not only demonstrate the strong synergy between the material's structural design and its practical sensing capabilities but also provide a versatile platform for environmental monitoring, quality control and other real-world analytical applications, offering valuable guidance for the development of next-generation electrochemical sensors.

2 Experimental section

2.1. Materials

All chemicals used were analytically pure and supplied by Sigma-Aldrich, used as received: $PdCl_2$ (99%), 2-methylimidazole ($C_4H_6N_2$) (99%), and hydrochloric acid (48%). Distilled water was used in this synthesis.

Hydroquinone (HQ), ascorbic acid (AA), catechol (CC), guaiacol, resorcinol (Res), glycine, bisphenol A (BA), potassium hexacyanoferrate (II) trihydrate ($K_4[Fe(CN)_6]\cdot 3H_2O$), potassium ferricyanide ($K_3[Fe(CN)_6]$), and all solvents were purchased from Sigma-Aldrich. Additional chemical reagents were obtained from Chimisi and Chimie Tunisie (Tunisia). The supporting electrolyte, phosphate-buffered saline (PBS), was prepared by dissolving 0.1 M KCl, 0.1 M KH_2PO_4, and K_2HPO_4 in deionized water, and its pH was modified to the desired level with HCl or NaOH.

2.2. Electrochemical measurements

Electrochemical measurements, including cyclic voltammetry (CV), electrochemical impedance spectroscopy (EIS), and differential pulse voltammetry (DPV), were conducted using an Autolab PGSTAT302N potentiostat/galvanostat (Eco Chemie, Netherlands) controlled *via* Nova 2.1 software. All experiments were carried out at room temperature in a standard three-electrode electrochemical cell, with a glassy carbon electrode (GCE), either bare or modified with IMPdCl, as the working electrode. A platinum wire and an Ag/AgCl (3 M KCl) electrode were used as the counter and reference electrodes, respectively. All electrochemical measurements were carried out in triplicate under identical conditions to ensure reproducibility and reliability of the results.

2.3. Crystal growth

The crystals of IMPdCl were synthesized by combining 2-methylimidazole, palladium chloride, and hydrochloric acid HCl in an aqueous solution with a molar ratio of 2 : 1. The mixture was subjected to magnetic stirring and heated for 20 minutes. After several days, the solution yielded colorless, block-shaped crystals, which were obtained by filtration and allowed to air-dry. The crystal growth was performed under ambient conditions without the use of an inert atmosphere, as the compound is stable to air and moisture. A single crystal was chosen for structural characterization *via* X-ray diffraction. The crystals exhibited stability under normal temperature and humidity conditions. The reaction afforded the compound $(C_4H_7N_2)[PdCl_3(H_2O)]$ in 85% yield under aqueous conditions (46% H_2O) at 25 °C, as shown below (Scheme 1).

2.4. Structure determination

A single colorless crystal of IMPdCl, with dimensions of 0.59 × 0.23 × 0.18 mm^3, was examined at 100 K using an XtaLAB Synergy Dualflex HyPix-Arc 100 diffractometer with MoKα radiation (λ = 0.71073 Å). The structure was solved by dual methods using ShelXT 2018/2 [68] and visualized through Olex2 1.5-ac5-024.[69] Refinement was carried out with ShelXL 2018/3 [70] employing full-matrix least-squares on F^2. IMPdCl crystallizes in the monoclinic $P2_1/c$ space group. Atomic coordinates and thermal parameters were refined iteratively, with all phenyl hydrogen atoms placed in geometrically constrained positions. The refinement converged to final values of $R_1 = 0.0389$, $wR_2 = 0.1063$, and GooF = 1.044. Complete crystallographic data are summarized in Table S1.

2.5. Preparation of the IMPdCl-modified glassy carbon electrode (GCE)

Before modification, the glassy carbon electrode (GCE) was cleaned using a multi-step procedure to ensure a clean and reproducible surface. Initially, the electrode was polished using a 0.05 μm alumina slurry on a polishing cloth until a mirror-like finish was obtained. The electrode was then rinsed thoroughly with deionized water to remove residual alumina particles, followed by ultrasonic cleaning in deionized water for 10 minutes to eliminate any remaining surface contaminants. For the fabrication of the IMPdCl-modified electrode, a drop-casting technique was used. Specifically, 1 mg of IMPdCl was dispersed in 1 mL of ethanol and ultrasonicated for 30 minutes to ensure a homogeneous suspension. A 10 μL aliquot of this dispersion was then drop-cast onto the surface of the pre-cleaned GCE. The modified electrode was left to air-dry at room temperature for 2 hours to allow complete solvent evaporation and ensure strong adhesion of the IMPdCl material to the electrode surface.

3 Results and discussion

3.1. Crystal structure

According to single-crystal X-ray diffraction, the compound crystallizes in the monoclinic system in the centrosymmetric $P2_1/c$ space group, with unit cell parameters $a = 9.0007(2)$ Å, $b = 14.7508(4)$ Å, $c = 7.4059(2)$ Å, $\beta = 94.084(2)°$, and $Z = 4$ (Table S1). The asymmetric unit consists of one protonated 2-methylimidazole cation $(C_4H_7N_2)^+$, one $[PdCl_3]^-$ anionic complex, and a crystallization water molecule (Fig. 1).

The Pd^{2+} center is coordinated by three chloride ligands and one water molecule, adopting a distorted octahedral geometry characteristic of d^8 Pd(II) complexes. It should be noted that this distortion is structural and not due to a Jahn–Teller effect, which requires orbital degeneracy absent in d^8 Pd(II). Instead, it arises from edge-sharing connectivity, ligand asymmetry, and crystal-packing forces. The Pd–Cl bond lengths vary from 2.5762(8) to 2.6508(9) Å, and the Pd–O bond measures 2.391(2) Å (Table S2). These distances and angular deviations are consistent with values reported for other Pd(II)–imidazole complexes. However, the degree of octahedral distortion is slightly more pronounced here due to the edge-sharing connectivity. The coordination geometry shows noticeable deviations from an ideal octahedron, with Cl–Pd–Cl angles varying between 88.10(3) and 172.16(3)° and O–Pd–Cl angles ranging from 81.11(6) to 173.36(6)°. These distortions arise from the edge-sharing connectivity between adjacent octahedra. The inorganic sublattice consists of infinite one-dimensional chains of edge-sharing $[PdCl_3(H_2O)]$ octahedra propagating along the c-axis (Fig. 2).

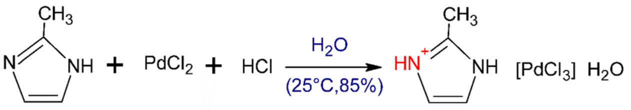

Scheme 1 Synthesis of the 1D $(C_4H_7N_2)[PdCl_3(H_2O)]$.

Within these chains, the Pd polyhedra adopt a zigzag configuration, interconnected by shared chloride ligands, which generates cohesive anionic sheets. These layers are interleaved with organic cations, which stabilize the framework through a dense hydrogen-bonding network (Fig. 3). Each water molecule functions as both donor and acceptor, forming O–H⋯Cl and N–H⋯O interactions, while the imidazolium cations provide additional N–H⋯Cl and weaker C–H⋯Cl contacts. A particularly notable feature is the N–H⋯O hydrogen bond linking the heterocycle to a water molecule, which subsequently bridges to Pd–Cl units, consolidating chain connectivity. Collectively, these interactions interconnect the inorganic chains into a robust three-dimensional supramolecular framework, with the $[PdCl_3]^-$ anion serving as a central hydrogen bond acceptor. The hydrogen bond distances (Table S3) fall within expected ranges, underscoring their structural relevance.

In addition to hydrogen bonding, π⋯π stacking interactions between adjacent imidazolium rings provide further stabilization, with a centroid-to-centroid distance of 3.5369 Å (Fig. 4), consistent with efficient aromatic overlap. These interactions, together with electrostatic attraction between the protonated organic cations and the anionic chains, reinforce the hybrid framework. The combination of coordination bonds, electrostatic interactions, hydrogen bonding, and π⋯π stacking leads

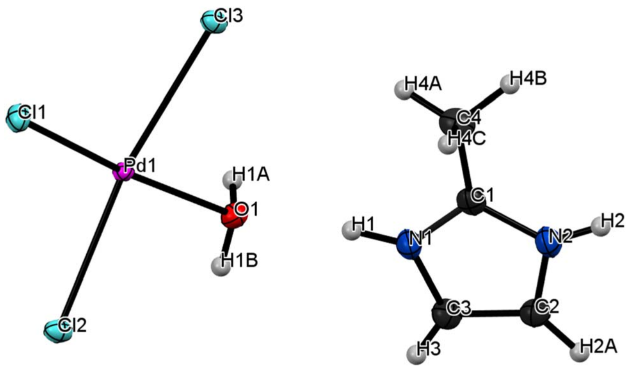

Fig. 1 The asymmetric unit of the crystal structure of $(C_4H_7N_2)[PdCl_3(H_2O)]$.

to a highly ordered three-dimensional organic–inorganic hybrid network.

Structurally, the crystal adopts a layered arrangement reminiscent of lamellar metal-halide systems, in which alternating organic and inorganic sheets are interleaved and stabilized by both coordination and supramolecular forces. In this architecture, strong metal-ligand bonds provide the backbone, while the hydrogen-bonding network and aromatic stacking critically stabilize the overall packing. This cooperative design not only enhances crystal stability but also modulates key physicochemical properties, including thermal robustness, solubility, and charge transport, which may underpin the observed semiconducting band gap (2.18 eV) and support potential applications in proton conduction, photocatalysis, and electrochemical sensing.

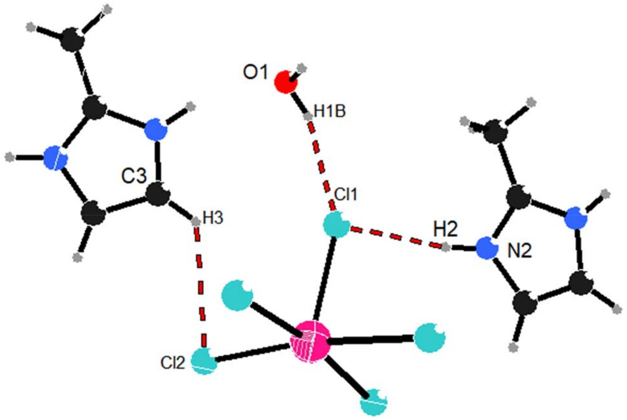

Fig. 3 Hydrogen-bonding pattern in the title compound.

3.2. IR spectroscopic characterization

To obtain a more detailed understanding of the phase composition and to support phase identification, the Fourier-transform infrared (FT-IR) spectrum of the layered perovskite $(C_4H_7N_2)[PdCl_3(H_2O)]$ was collected in the spectral region from 400 to 4000 cm^{-1}(Fig. 5) and analyzed by comparison with previously reported perovskite compounds.[71–73]

The spectrum exhibits several distinct absorption bands characteristic of the 2-methylimidazole $(C_4H_6N_2)$ ligand, revealing the internal vibrational modes of this heterocyclic organic cation, which are discussed in detail below. A broad and intense band in the region of 3400–3200 cm^{-1} is assigned to the stretching vibration of the N–H bond within the imidazole ring. The broad nature of this band is indicative of hydrogen bonding, either intermolecular or intramolecular, which is common in imidazole-containing systems. In the region of 3100–3000 cm^{-1}, multiple absorption bands are observed and correspond to the aromatic C–H stretching vibrations of the imidazole ring. Meanwhile, the presence of the methyl substituent at the 2-position is confirmed by the aliphatic C–H

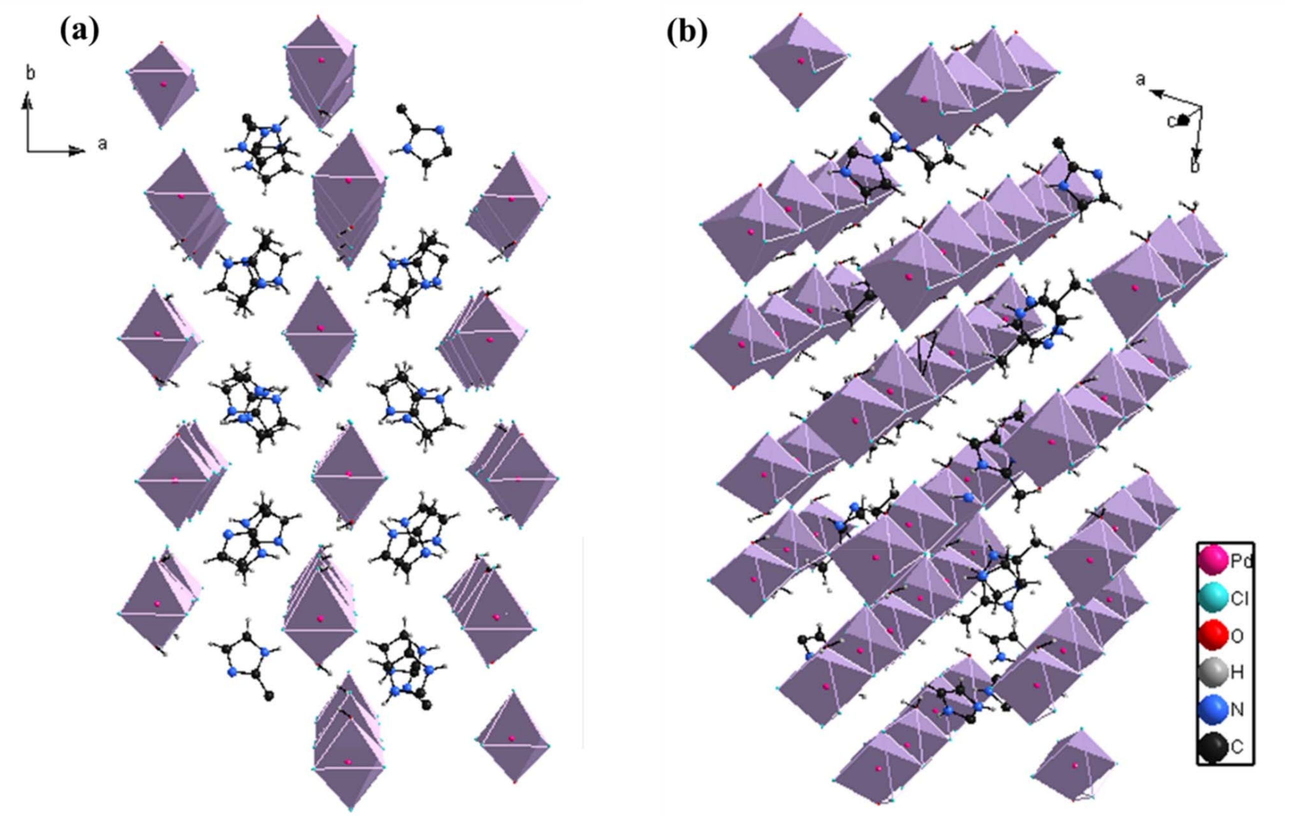

Fig. 2 Crystallographic representation of $(C_4H_7N_2)[PdCl_3(H_2O)]$: (a) arrangement viewed along the *c*-axis; (b) layered organization of the compound.

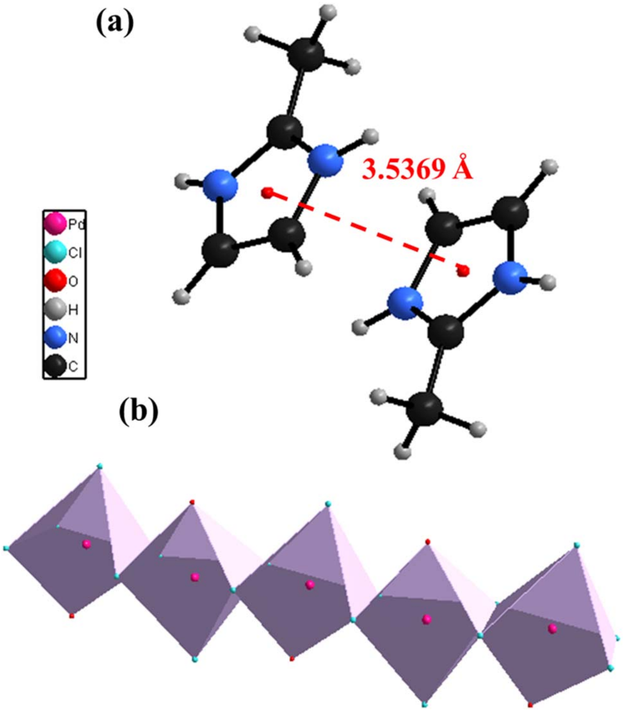

Fig. 4 (a) The π–π interactions between the chains of the aromatic rings $C_4H_7N_2$ (b) edge sharing $[PdCl_5(H_2O)]$ octahedral chain.

stretching vibrations detected between 2960 and 2870 cm^{-1}. A prominent absorption band around 1600 cm^{-1} is attributed to the C=N stretching vibration, possibly coupled with C=C stretching modes of the aromatic ring. This band is a key spectral feature for confirming the aromatic character and the electronic delocalization within the imidazole ring. Additional bands in the 1500–1400 cm^{-1} region are assigned to in-plane bending vibrations of the C–H bonds in both the aromatic ring and the methyl group. The absorption features observed between 1300 and 1000 cm^{-1} are mainly associated with C–N stretching vibrations and N–H in-plane bending modes, which are highly sensitive to substitution and coordination effects. Furthermore, the region between 900 and 600 cm^{-1} contains several well-defined bands that correspond to out-of-plane bending modes of C–H bonds, which are typical for substituted aromatic systems. Notably, an intense absorption band appearing near 500–450 cm^{-1} may be indicative of metal-ligand interactions, particularly if the compound forms a coordination complex with a transition metal such as Pd(II). This band could correspond to M–Cl or M–N stretching modes, depending on the coordination environment. Overall, the FT-IR spectrum confirms the presence and structural integrity of the 2-methylimidazole ligand, offering initial evidence of its potential coordination to the metal center *via* nitrogen atoms.

3.3. UV-visible absorption spectrum and optical band gap analysis

To investigate electronic transitions, we conducted a solid-state optical absorption analysis of the material. The diffuse reflectance spectrum was measured and subsequently converted into an absorption spectrum using the Kubelka–Munk (K–M) function, as shown in this equation:

$$F(R) = \frac{(1-R)^2}{2R} = \frac{K}{S} \propto 2\alpha$$

where R represents the sample reflectance, K is the Kubelka–Munk absorption coefficient, and S is the scattering coefficient. The absorption spectra in the UV-vis region (200–1100 nm) were measured, as illustrated in Fig. 6.

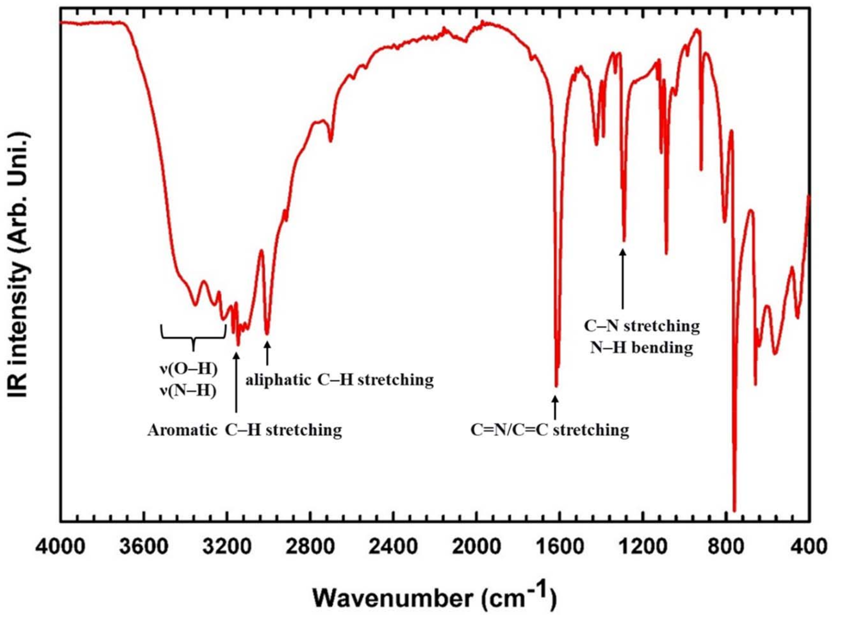

Fig. 5 Infrared spectrum of the title compound.

The absorption spectrum (Fig. 6a) shows intense UV absorption around 200 nm, with additional peaks at 230 and 315 nm, corresponding to ligand-to-metal charge transfer (LMCT) and intra-ligand transitions involving the 2-methylimidazolium ring and the chloride-coordinated Pd(II) center. The palladium atom adopts a distorted octahedral coordination geometry, which plays a significant role in shaping the electronic transitions observed in the spectrum. The Tauc plot (Fig. 6b), constructed from the diffuse reflectance data using the Kubelka–Munk function, indicates an optical band gap (E_g^{opt}) of 2.18 eV, consistent with semiconducting behavior. This moderate band gap arises from the combined effects of the electronic characteristics of the octahedral Pd(II) coordination environment and the extended supramolecular architecture, notably involving hydrogen bonding and $\pi\cdots\pi$ stacking interactions. These structural features emphasize the pivotal role of both coordination geometry and non-covalent interactions in modulating the material's optoelectronic properties, highlighting its potential for applications in photocatalysis, chemical sensing and hybrid proton-conducting systems.

3.4. Electrochemical analysis of IMPdCl-modified GCE

The electrochemical performance of both unmodified glassy carbon electrodes (GCE) and GCE modified with IMPdCl was systematically investigated using cyclic voltammetry (CV) and electrochemical impedance spectroscopy (EIS). As shown in Fig. 7a, the unmodified GCE exhibited weak and poorly defined redox peaks, reflecting its inherently low electrocatalytic activity. In contrast, the IMPdCl2-modified electrodes displayed significantly enhanced redox currents, demonstrating that the incorporation of IMPdCl markedly improves electron transfer kinetics at the electrode–electrolyte interface. The observed enhancement arises from the unique features of the IMPdCl complex, which improve conductivity, enable efficient charge transport, and contribute to enhanced redox performance. EIS measurements were performed over 0.05 Hz to 100 kHz at a 10 mV amplitude, offering additional information on interfacial phenomena. High-frequency data reflect charge transfer resistance and double-layer capacitance, while low-frequency behavior is controlled by ionic diffusion. As shown in Fig. 7b, the Nyquist plot of the IMPdCl-modified electrode displays a significantly smaller semicircle than that of the bare GCE, indicating a marked decrease in charge transfer resistance. These results confirm that modification with IMPdCl significantly enhances electron transfer capabilities and improves the overall electrochemical performance of the electrode.

The effect of scan rate on the electrochemical response of the IMPdCl-modified glassy carbon electrode (IMPdCl/GCE) was investigated *via* cyclic voltammetry (CV) in a 5 mM $[Fe(CN)_6]^{3-/4-}$ solution, as shown in Fig. 8a. CV measurements at scan rates between 40 and 160 mV s^{-1} revealed that both anodic and cathodic peak currents increased proportionally with the scan rate, indicating enhanced diffusion of redox-active species to the electrode surface. This behavior is characteristic of a quasi-reversible redox process, where electron transfer kinetics and mass transport jointly affect the electrochemical response. Fig. 8b shows a linear correlation between the peak current (I_p) and the square root of the scan rate ($\nu^{1/2}$), confirming that the redox process is predominantly diffusion-controlled.

These results, in line with previous CV and EIS findings, validate the beneficial role of IMPdCl in promoting efficient electron transfer. This enhancement highlights the suitability of the IMPdCl-modified electrode for use in high-performance electrochemical sensing applications.

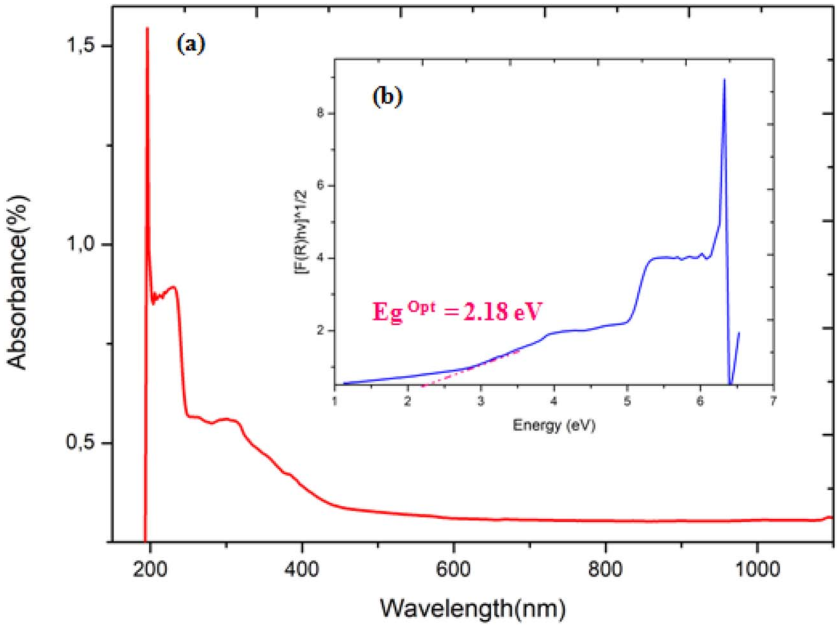

Fig. 6 (a) K–M absorption spectrum and (b) Tauc plot for the direct gap calculation of $(C_4H_7N_2)[PdCl_3(H_2O)]$.

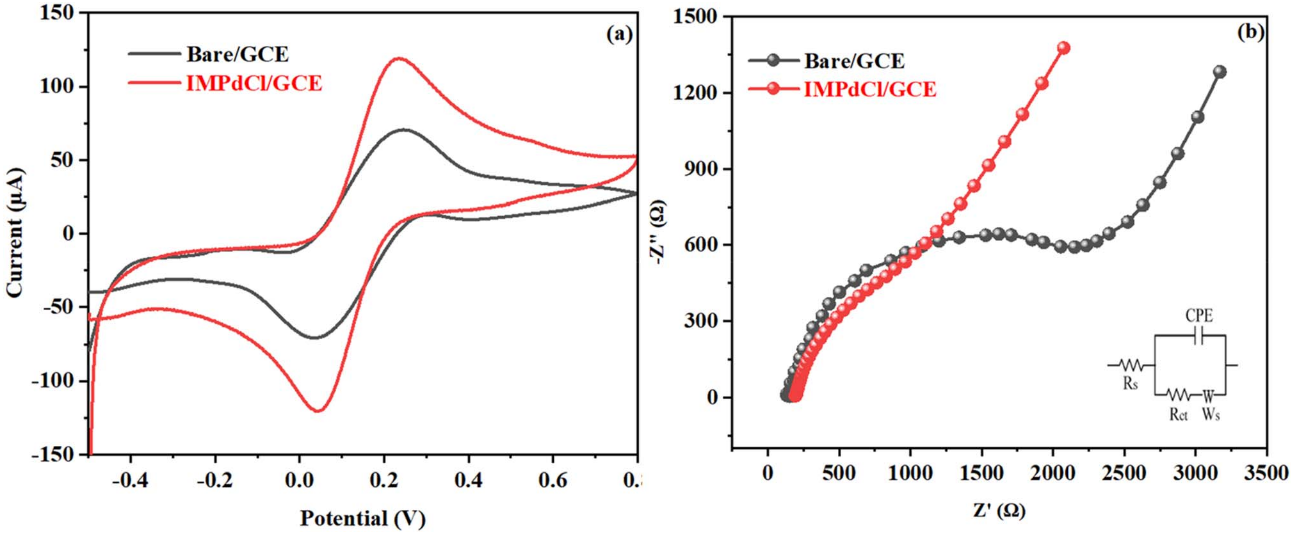

Fig. 7 (a) Cyclic voltammetry (CV) curves and (b) electrochemical impedance spectroscopy (EIS) spectra of the bare glassy carbon electrode (GCE) and IMPdCl-modified GCE, recorded in a 5 mM $[Fe(CN)_6]^{3-/4-}$ solution containing 0.1 M KCl as the supporting electrolyte. CV was performed at a scan rate of 100 mV s^{-1}. EIS measurements were carried out over a frequency range of 0.05 Hz to 100 kHz with an applied AC amplitude of 10 mV.

The linear regression was obtained from the correlation between the scan rate (ν, mV s^{-1}) and the anodic and cathodic peak currents (I_{pa} and I_{pc})

$$I_{pa}\ (\mu A) = 13.984\ \nu^{1/2}\ (mV\ s^{-1}) + 20.136\ (R^2 = 0.998) \tag{1}$$

$$I_{pc}\ (\mu A) = -13.173\ \nu^{1/2}\ (mV\ s^{-1}) - 12.133\ (R^2 = 0.997) \tag{2}$$

The electroactive areas of GCE and $(C_4H_7N_2)[PdCl_3(H_2O)]$/GCE were then estimated using the Randles–Ševčík equation:[41,74]

$$I_p = (2.69 \times 10^5) \times n^{3/2} \times A \times D^{1/2} \times C \times \nu^{1/2} \tag{3}$$

In the equation, I_p represents the peak current (A), n is the number of electrons involved in the redox reaction, A denotes the electroactive surface area (cm^2), D is the diffusion coefficient of $[Fe(CN)_6]^{3-/4-}$ in 0.1 M KCl (7.6×10^{-6} cm^2 s^{-1}), ν is the scan rate (V s^{-1}), and C is the bulk concentration (mol cm^{-3}). Surface modification of the glassy carbon electrode (GCE) with IMPdCl significantly increased the electrochemically active surface area (EASA), with the modified electrode exhibiting an EASA of 0.205 cm^2 compared to the geometric area of the bare GCE (0.112 cm^2). This enhancement indicates that the modification not only increases surface roughness but also promotes electron transfer by providing additional active sites for electrochemical reactions. The electrochemical response of 10 μM

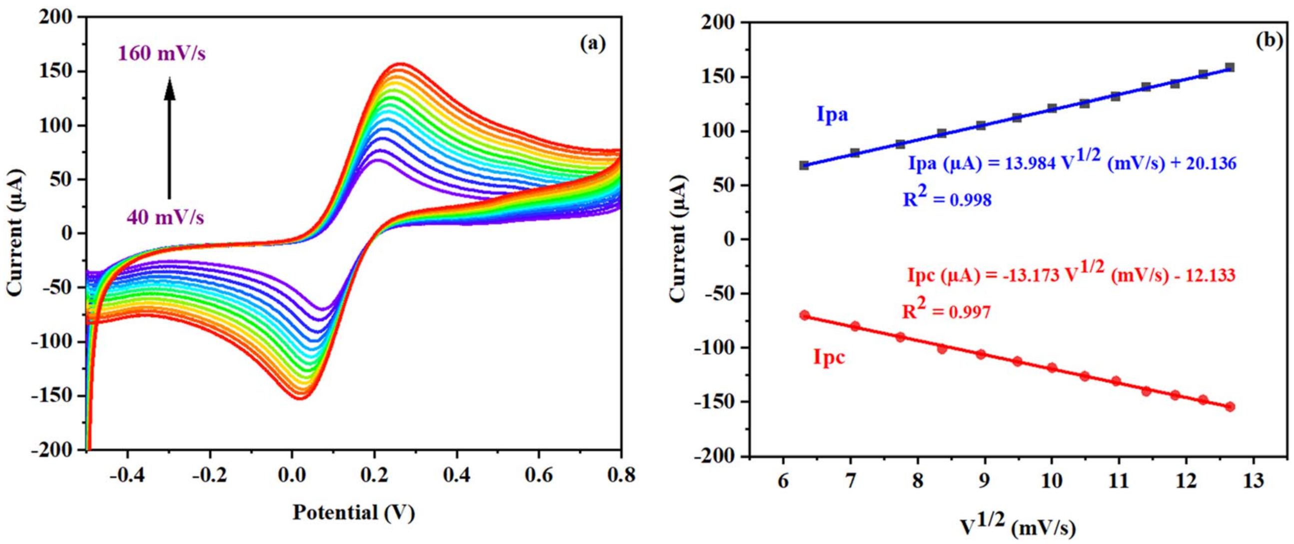

Fig. 8 (a) CVs curves obtained at the different scanning rates (40–160 mV s^{-1}) for IMPdCl/GCE in a 5 mM $[Fe(CN)_6]^{3-/4-}$ solution and (b) the respective calibration plots of $\nu^{1/2}$ *vs.* I_{pa} and I_{pc}.

hydroquinone (HQ) in 0.1 M phosphate-buffered saline (PBS, pH 7.4) was investigated using differential pulse voltammetry (DPV) with different electrode configurations. As depicted in Fig. 9, the unmodified GCE displayed weak and poorly defined oxidation peaks, demonstrating its limited sensitivity toward HQ detection.

Compared to the bare electrode, the IMPdCl-modified GCE displayed markedly increased oxidation currents, demonstrating enhanced electrocatalytic efficiency. This improvement can be attributed to the increased electroactive surface area and superior electron transfer kinetics imparted by the IMPdCl layer. The high conductivity and catalytic activity of IMPdCl enhance the interaction between hydroquinone (HQ) molecules and the electrode surface, yielding stronger and more well-defined electrochemical signals. These results emphasize the considerable potential of IMPdCl as a highly sensitive and effective material for the electrochemical detection of HQ in aqueous solutions.

3.5. Effect of pH

The influence of the supporting electrolyte's pH on the electrochemical response of the IMPdCl/GCE sensor was systematically investigated by differential pulse voltammetry (DPV) over a pH range of 3.0–9.0. As shown in Fig. 10, the oxidation peak current gradually increased with increasing pH, reaching a maximum at pH 7.4.

The observed behavior indicates a synergistic influence of proton concentration and the electrode surface charge on the electrochemical oxidation process of HQ. At lower pH levels, abundant protons facilitate the oxidation reaction, whereas the electrode surface may bear positive charges that affect adsorption dynamics. Conversely, beyond pH 7.4, the peak current diminished, likely attributable to a reduction in proton availability, which is essential for the redox mechanism, as well as possible alterations in the speciation of HQ and changes in the electrode-analyte interfacial interactions. These findings underscore the critical balance between proton-mediated electron transfer and surface chemistry in optimizing sensor response. As a result, PBS at pH 7.4 was identified as the most suitable supporting electrolyte, providing a consistent and stable medium that enhances the sensitivity of the sensor for HQ detection in all further tests.

3.6. DPV analysis of hydroquinone (HQ)

The electrochemical response of the IMPdCl/GCE electrode to sequential additions of hydroquinone (HQ) is illustrated in Fig. 11a. Notably, the sensor exhibited two distinct linear dynamic ranges: 0.02–1.5 μM and 1.5–10 μM, with an impressive detection limit as low as 0.02 μM (s/n = 3). This dual-range behavior highlights the IMPdCl-modified electrode's remarkable sensitivity and versatility for urea detection over both trace and higher concentration levels. In the lower concentration range (0.02–1.0 μM), the calibration curve is described by the equation:

$$I_{\mathrm{pa}}\ (\mu\mathrm{A}) = 1.992 \times C_{(\mathrm{hydroquinone\ (HQ)})}\ (\mu\mathrm{M}) + 30.909\ (\mu\mathrm{M}) \quad (4)$$

With a strong correlation ($R^2 = 0.98$), the sensor shows high accuracy for trace-level HQ detection. The observed behavior suggests that the process is adsorption-controlled, with the electrode's abundant active sites facilitating efficient electron transfer and improved signal response at low analyte concentrations. In the higher linear range (1–10 μM), the calibration curve follows:

$$I_{\mathrm{pa}}\ (\mu\mathrm{A}) = 22.563 \times C_{(\mathrm{hydroquinone\ (HQ)})}\ (\mu\mathrm{M}) + 0.2169\ (\mu\mathrm{M}) \quad (5)$$

With an equally high correlation coefficient ($R^2 = 0.99$), as shown in Fig. 11b.

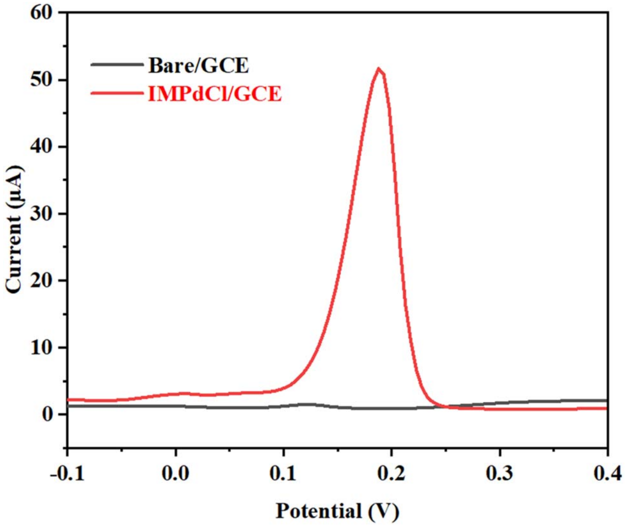

Fig. 9 Differential pulse voltammetry (DPV) of 10 μM hydroquinone (HQ) at the bare GCE and IMPdCl/GCE in 0.1 M phosphate buffer solution PBS (pH = 7.4).

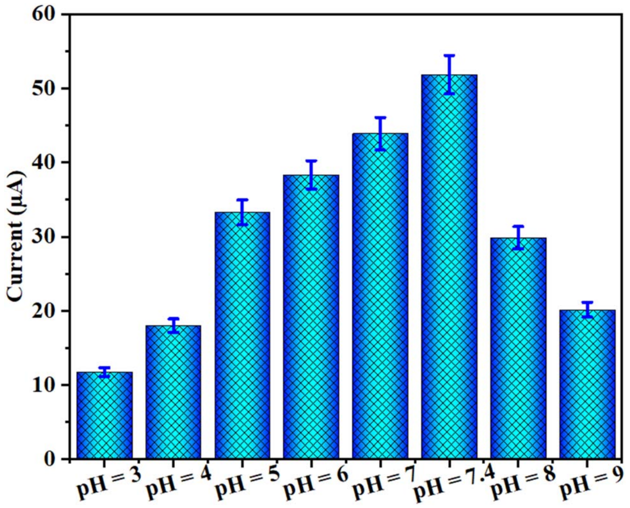

Fig. 10 Effect of solution pH on the current response of the IMPdCl/GCE electrode in 0.1 M phosphate buffer solution containing 10 μM hydroquinone (HQ).

Table 1 Comparison of the analytical performance with other methods using different electrode materials for the determination of hydroquinone (HQ)

Electrode material	Linear range (μM)	Detection limit (μM)	Reference
GS/BMIMPF$_6$/GCE	500–50.000	10	75
Graphene-chitosan/GCE	1.000–300.000	750	76
ECF-CPE	1.000–200.000	400	77
Pt–Au–OSi@CS/GCE	30–172.980	10	78
NA-COGH	400–600.000	19	79
Polydopamine-RGO	1.000–2.500.000	62	80
GMC/GCE	2.000–5.000	370	81
GO-mesoporous MnO$_2$/GCE	10–700	7	82
GR-P4VP/GCE	100–10.000	8.1	83
ER(GO-TT-CNT)	10–200.000	7.61	84
IMPdCl/GCE	0.02–10	0.02	This work

This range likely reflects a diffusion-controlled process, in which the gradual saturation of active sites causes the rate-limiting step to become the transport of hydroquinone (HQ) molecules from the bulk solution to the electrode surface. These two distinct linear regions highlight the electrode's excellent reliability, sensitivity, and precision for hydroquinone (HQ) quantification over a wide concentration spectrum, underscoring its suitability for multiple analytical purposes. Moreover, the consistently low detection limit of 0.02 μM further confirms the remarkable performance and practical utility of the IMPdCl/GCE sensor in the sensitive electrochemical detection of hydroquinone (HQ). This combination of broad linear range, high correlation coefficients, and ultralow detection thresholds demonstrates that the sensor is well-suited for trace analysis in complex real samples, offering a robust platform for environmental monitoring, biomedical diagnostics, and food safety assessments. The electro-oxidation mechanism of hydroquinone (HQ) at the IMPdCl-GCE involves a fast and reversible two-electron, two-proton transfer process converting HQ to benzoquinone (BQ). Upon applying an anodic potential, HQ molecules adsorbed on the electrode surface undergo oxidation, releasing two protons and two electrons according to the reaction HQ $\rightleftharpoons$ BQ + 2H$^+$ + 2e$^-$ (Scheme 2).

The IMPdCl modifier significantly enhances this process by increasing the effective surface area, facilitating electron transfer, and stabilizing the redox couple. This catalytic behavior results in significantly higher peak currents and a reduced overpotential compared to the bare GCE. The electrochemical response shows well-defined redox peaks with

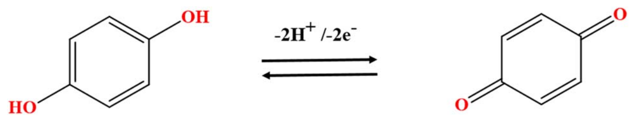

Scheme 2 Electro-oxidation mechanism of hydroquinone (HQ).

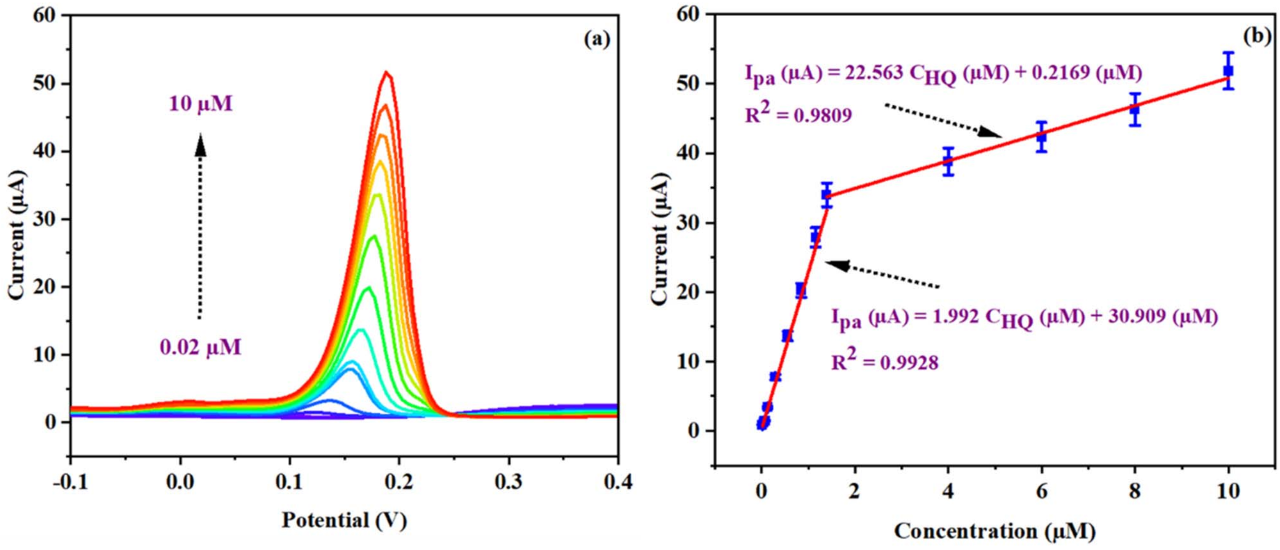

Fig. 11 (a) Differential pulse voltammetry (DPV) response of hydroquinone (HQ) recorded on various modified electrodes, including IMPdCl/GCE. (b) Corresponding calibration curves for creatinine using IMPdCl/GCE in 0.1 M phosphate-buffered saline (PBS) at pH 7.4.

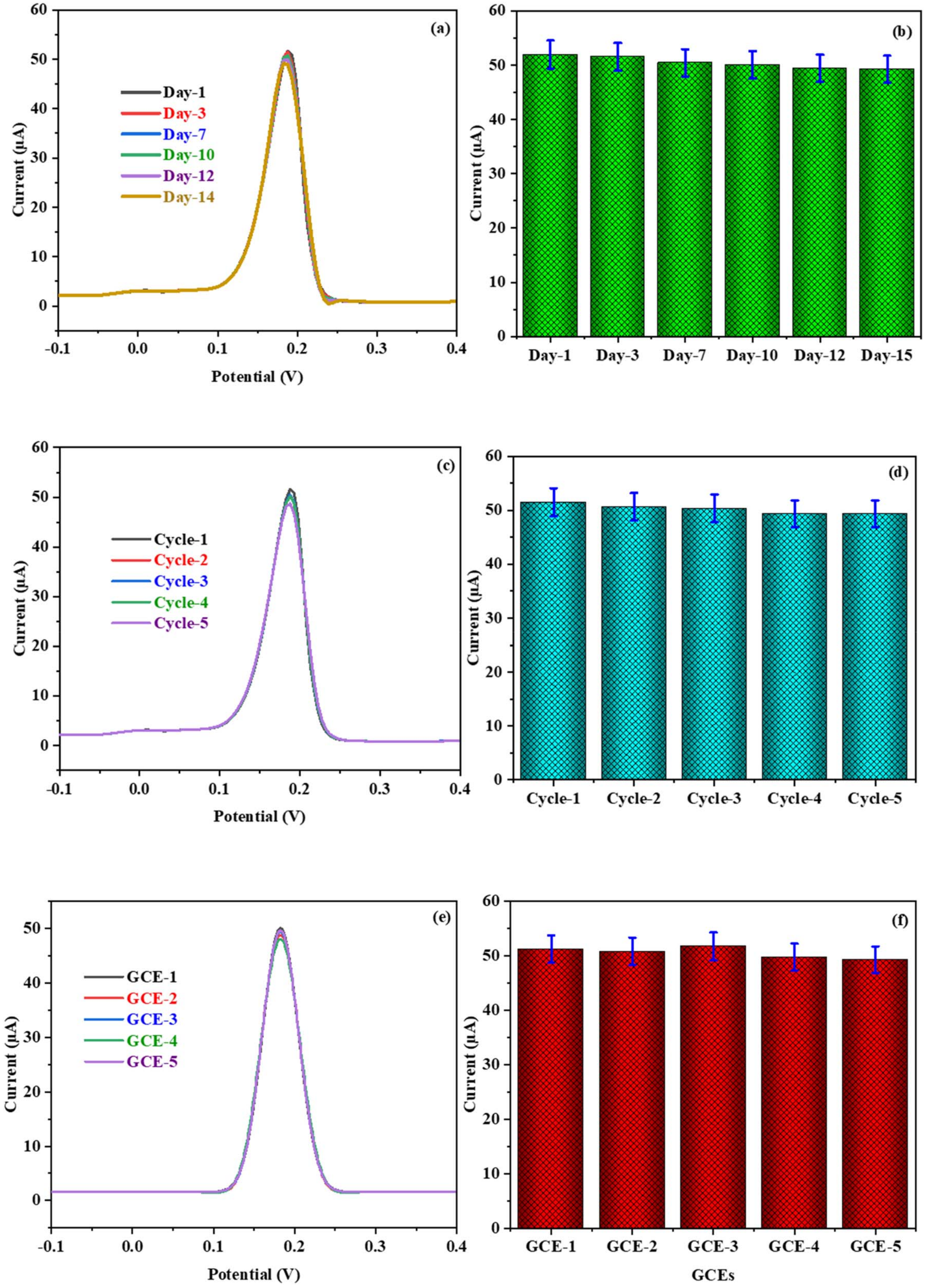

Fig. 12 (a) Differential pulse voltammetry (DPV) curves demonstrating the long-term storage stability of the IMPdCl-modified electrode over a 14-day period. (b) Current response as a function of storage time (c) DPV responses illustrating short-term repeatability across five consecutive measurements, with electrode regeneration between each run. (d) Assessment of signal stability during five successive measurements (e) DPV curves obtained using five independently fabricated IMPdCl-modified electrodes under identical conditions. (f) Evaluation of fabrication reproducibility of peak current responses recorded across different electrodes.

minimal peak-to-peak separation, reflecting rapid electron transfer between HQ and the electrode surface facilitated by IMPdCl. Table 1 demonstrates that the IMPdCl-modified glassy carbon electrode exhibits superior analytical performance for hydroquinone (HQ) detection compared to previously reported materials and techniques. Notably, this electrode exhibits an extremely low detection limit of 0.02 μM and a broad linear response range. These results highlight the synergistic effect of the IMPdCl complex in promoting efficient electron transfer and enhancing catalytic activity, making it a promising platform for the sensitive and selective electrochemical determination of HQ in real samples.

3.7. Stability, repeatability, and reproducibility of the IMPdCl-modified electrode

The long-term stability of the IMPdCl-modified glassy carbon electrode (IMPdCl/GCE) was thoroughly evaluated over a period of 14 days. Differential pulse voltammetry (DPV) measurements were performed at defined time intervals (days 1, 3, 7, 10, 12 and 14) to monitor the sensor's performance. As shown in Fig. 12a, and quantitatively summarized in Fig. 12b, the electrode maintained more than 94% of its initial current response after 14 days of storage under ambient laboratory conditions. This strong retention of electrochemical activity highlights the excellent adhesion, stability and robustness of the IMPdCl nanocomposite coating, affirming its potential for extended use without significant loss of sensitivity or functionality. The short-term repeatability of the electrode response was further examined through multiple successive measurements in a 10 μM hydroquinone (HQ) solution prepared in 0.1 M phosphate buffer (PBS, pH 7.4). Five independent DPV scans were conducted using the same IMPdCl/GCE under optimized conditions. To ensure proper regeneration between each cycle, the electrode was soaked in PBS for 20 minutes to remove adsorbed analyte molecules, thoroughly rinsed with distilled water, and allowed to air-dry for one hour at room temperature. To simulate continuous operation, an additional set of five consecutive DPV scans was conducted without any regeneration step between measurements. As depicted in Fig. 12(c) and (d), the peak current values remained highly stable across the measurement series, with a relative standard deviation (RSD) is 1.82%, demonstrating remarkable repeatability and consistent electrochemical performance during successive analyses. The reproducibility of the electrode fabrication process was also validated. Five individually prepared IMPdCl-modified electrodes were fabricated using the same protocol and tested in a 10 μM HQ solution under identical conditions. The resulting DPV signals exhibited excellent consistency, as illustrated in Fig. 12(e) and (f), with a low RSD of 2.03% in peak current values

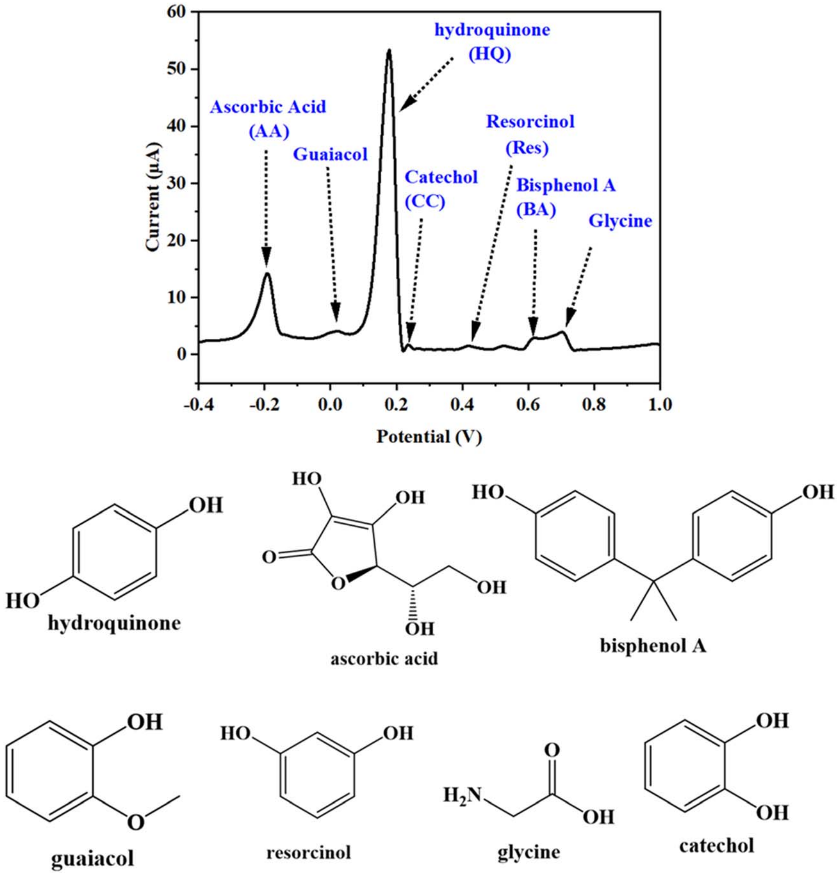

Fig. 13 Differential pulse voltammetry (DPV) curves recorded for 10 μM hydroquinone (HQ) with and without the addition of 100 μM ascorbic acid (AA), catechol (CC), guaiacol, resorcinol (Res), glycine, and bisphenol A (BA).

across all electrodes. These results confirm the high reproducibility of the modification procedure and underscore the reliability of the sensor platform for scalable and routine applications in electrochemical sensing.

3.8. Interference study of the IMPdCl-modified electrode

The selectivity of the IMPdCl-modified glassy carbon electrode (IMPdCl/GCE) towards hydroquinone (HQ) was systematically evaluated in the presence of various potentially interfering substances commonly encountered. Specifically, ascorbic acid (AA), catechol (CC), guaiacol, resorcinol (Res), glycine, and bisphenol A (BA) were selected as representative electroactive compounds. Electrochemical measurements were performed under optimized conditions in 0.1 M phosphate buffer solution (PBS, pH 7.4) containing 10 μM HQ. Each interfering substance was added at a tenfold higher concentration (100 μM) to rigorously challenge the sensor's selectivity and robustness.

As illustrated by the DPV curves in Fig. 13, the introduction of these potential interferents produced only negligible variations in the HQ peak current response, confirming that the IMPdCl-modified electrode effectively discriminates hydroquinone even in the presence of excess amounts of structurally similar or electroactive compounds.

This minimal deviation in signal underscores the sensor's excellent anti-interference capability and high analytical selectivity. Collectively, these results demonstrate that the IMPdCl/GCE retains reliable and accurate electrochemical detection of hydroquinone in complex environmental or biological matrices, reinforcing its suitability for practical applications in trace analysis and real-sample monitoring.

3.9. Practical applicability and validation of the sensor for real sample analysis

The real-world performance and potential applications of the synthesized IMPdCl-modified glassy carbon electrode (IMPdCl/GCE) were rigorously assessed by quantifying hydroquinone (HQ) concentrations in real water matrices, including tap water and bottled mineral water samples spiked with predetermined HQ levels. All analyses were conducted at room temperature under optimized electrochemical conditions. As summarized in Table 2, the sensor exhibited outstanding recovery rates ranging from 96.4% to 105.2%, underscoring its excellent precision, reliability, and suitability for complex aqueous environments. The relative standard deviations (RSD) remained consistently below 3.0%, confirming the high reproducibility of the measurements. The results demonstrate that the developed sensor provides rapid, precise and selective hydroquinone detection in environmental matrices, eliminating the requirement for elaborate sample preparation. Its robust analytical performance highlights its potential for routine monitoring and quality control applications in environmental analysis.

Table 2 Determination of hydroquinone (HQ) in real water samples using the IMPdCl/GCE sensor

Sample type	Added (μM)	Found (μM)	Recovery (%)	RSD (%)
Tap water	2.00	2.09	104.5	2.7
	8.00	7.85	98.1	2.3
Mineral water	2.00	1.93	96.4	2.5
	8.00	8.42	105.2	1.9

4 Conclusion

In this study, a new 1D organic–inorganic hybrid compound, $(C_4H_7N_2)[PdCl_3(H_2O)]$, was prepared and its structure thoroughly characterized. X-ray diffraction showed a chain-like structure formed by edge-sharing $[PdCl_3(H_2O)]$ units, stabilized by hydrogen bonds and $\pi\cdots\pi$ interactions. Infrared spectroscopy confirmed key functional groups, while UV-vis analysis exhibited intense UV absorption along with an optical band gap of 2.18 eV, indicating semiconducting properties. The IMPdCl-modified glassy carbon electrode developed in this study demonstrates exceptional analytical performance for the electrochemical detection of hydroquinone (HQ). With a detection limit as low as 0.02 μM, wide linear ranges spanning 0.02–10 μM, and excellent selectivity, the sensor effectively resists interference from high levels of common substances. Comprehensive evaluation of stability, repeatability, and reproducibility confirmed the robustness and reliability of the electrode modification process. Furthermore, the sensor showed outstanding recovery rates when applied to real water samples, underscoring its practical applicability in environmental surveillance and quality management. These findings underscore the considerable potential of the IMPdCl/GCE platform as a sensitive, selective, and user-friendly tool for routine electrochemical analysis of hydroquinone and related analytes in complex matrices.

Author contributions

Sarra Bougossa: formal analysis, writing – original draft; Naoufel Ben Hamadi: data curation, investigation; Jassem Wannassi: data curation, writing; Noureddine Mhadhbi: writing, validation; Jeanneau Erwann: data curation, formal analysis; Ahlem Guesmi: formal analysis, visualization; Lotfi Khezami: data curation, investigation, Houcine Barhoumi: review & editing, data curation; Houcine Naïli: project administration, validation, supervision.

Conflicts of interest

The authors declare that they have no known competing financial interests or personal relationships that could have appeared to influence the work reported in this paper.

Data availability

CCDC 2482370 $(C_4H_7N_2)[PdCl_3(H_2O)]$ contains the supplementary crystallographic data for this paper.[85]

The data that supported the findings of this study were available upon reasonable request.

Supplementary information (SI): crystal data, molecular geometry, and hydrogen-bond parameters of $(C_4H_7N_2)[PdCl_3(H_2O)]$. See DOI: https://doi.org/10.1039/d5ra08631k.

Funding

This work was supported and funded by the Deanship of Scientific Research at Imam Mohammad Ibn Saud Islamic University (IMSIU) (grant number IMSIU-DDRSP2602).

References

1 S. K. Tulashie, V. Ackom, E. B. Baidoo, G. Acquah, B. Fialor and E. M. Alale, Changing Skin: The Prevalence, Impact, and Risks of Skin Bleaching Among African Women, *J. Racial Ethn. Health Dispar.*, 2025, **12**, 1–15, DOI: 10.1007/s40615-025-02695-0.

2 Z. D. Draelos, Skin lightening preparations and the hydroquinone controversy, *Dermatol. Ther.*, 2007, **20**, 308–313, DOI: 10.1111/j.1529-8019.2007.00144.x.

3 Z. D. Draelos, G. Deliencourt-Godefroy and L. Lopes, An effective hydroquinone alternative for topical skin lightening, *J. Cosmet. Dermatol.*, 2020, **19**, 3258–3261, DOI: 10.1111/jocd.13771.

4 B. Desmedt, G. Ates, P. Courselle, J. O. De Beer, V. Rogiers, B. Hendrickx, E. Deconinck and K. De Paepe, In vitro Dermal Absorption of Hydroquinone: Protocol Validation and Applicability on Illegal Skin-Whitening Cosmetics, *Skin Pharmacol. Physiol.*, 2016, **29**, 300–308, DOI: 10.1159/000454719.

5 B. Desmedt, P. Courselle, J. O. De Beer, V. Rogiers, M. Grosber, E. Deconinck and K. De Paepe, Overview of skin whitening agents with an insight into the illegal cosmetic market in Europe, *J. Eur. Acad. Dermatol. Venereol.*, 2016, **30**, 943–950, DOI: 10.1111/jdv.13595.

6 I. M. Fabian, E. S. Sinnathamby, C. J. Flanagan, A. Lindberg, B. Tynes, R. A. Kelkar, G. Varrassi, S. Ahmadzadeh, S. Shekoohi and A. D. Kaye, *Cureus*, 2023, **15**, 48840, DOI: 10.7759/cureus.48840.

7 I. Duarte, R. F. Mendonca, K. L. Korkes, R. Lazzarini and M. F. S. Hafner, Nickel, chromium and cobalt: the relevant allergens in allergic contact dermatitis. Comparative study between two periods: 1995-2002 and 2003-2015, *An. Bras. Dermatol.*, 2018, **93**, 59–62, DOI: 10.1590/abd1806-4841.20186047.

8 M. G. Ahlstrom, J. P. Thyssen, M. Wennervaldt, T. Menne and J. D. Johansen, Nickel allergy and allergic contact dermatitis: A clinical review of immunology, epidemiology, exposure, and treatment, *Contact Dermat.*, 2019, **81**, 227–241, DOI: 10.1111/cod.13327.

9 D. Bregnbak, J. D. Johansen, M. S. Jellesen, C. Zachariae, T. Menne and J. P. Thyssen, Chromium allergy and dermatitis: prevalence and main findings, *Contact Dermat.*, 2015, **73**, 261–280, DOI: 10.1111/cod.12436.

10 S. J. L. Linde, A. Franken and J. L. du Plessis, *Int. Arch. Occup. Environ. Health*, 2023, **96**, 259–270, DOI: 10.1007/s00420-022-01921-0.

11 J. J. Hostynek, R. S. Hinz, C. R. Lorence, M. Price and R. H. Guy, Metals and the skin, *Crit. Rev. Toxicol.*, 1993, **23**, 171–235, DOI: 10.3109/10408449309117116.

12 M. Matsumoto, H. Todo, T. Akiyama, M. Hirata-Koizumi, K. Sugibayashi, Y. Ikarashi, A. Ono, A. Hirose and K. Yokoyama, Risk assessment of skin lightening cosmetics containing hydroquinone, *Regul. Toxicol. Pharmacol.*, 2016, **81**, 128–135, DOI: 10.1016/j.yrtph.2016.08.005.

13 S. Chuenjitt, A. Kongsuwan, C. H. Phua, J. Saichanapan, A. Soleh, K. Saisahas, K. Samoson, S. Wangchuk, K. Promsuwan and W. Limbut, *Electrochim. Acta*, 2022, **434**, 141272, DOI: 10.1016/j.electacta.2022.141272.

14 Y. Zheng, X. Du, L. Zhang, T. Jia, H. Zhang, B. Peng, Y. Hao, Z. Tong, D. Che and S. Geng, Hydroquinone-induced skin irritant reaction could be achieved by activating mast cells via mas-related G protein–coupled receptor X2, *Exp. Dermatol.*, 2023, **32**, 436–446, DOI: 10.1111/exd.14723.

15 C. Singh and A. Paul, Physisorbed Hydroquinone on Activated Charcoal as a Supercapacitor: An Application of Proton-Coupled Electron Transfer, *J. Phys. Chem. C*, 2015, **119**, 11382–11390, DOI: 10.1021/acs.jpcc.5b01322.

16 I. Sires, E. Brillas, M. A. Oturan, M. A. Rodrigo and M. Panizza, Electrochemical advanced oxidation processes: today and tomorrow. A review, *Environ. Sci. Pollut. Res. Int.*, 2014, **21**, 8336–8367, DOI: 10.1007/s11356-014-2783-1.

17 M. Cheng, X. Yang, C. Chen, J. Zhao, F. Zhang and L. Sun, Dye-sensitized solar cells based on hydroquinone/benzoquinone as bio-inspired redox couple with different counter electrodes, *Phys. Chem. Chem. Phys.*, 2013, **15**, 15146–15152, DOI: 10.1039/C3CP51980E.

18 W. Gao and C. Legido-Quigley, Fast and sensitive high performance liquid chromatography analysis of cosmetic creams for hydroquinone, phenol and six preservatives, *J. Chromatogr. A*, 2011, **1218**, 4307–4311, DOI: 10.1016/j.chroma.2011.04.064.

19 Sirajuddin, M. I. Bhanger, A. Niaz, A. Shah and A. Rauf, Ultra-trace level determination of hydroquinone in waste photographic solutions by UV-vis spectrophotometry, *Talanta*, 2007, **72**, 546–553, DOI: 10.1016/j.talanta.2006.11.021.

20 O. Brito de Oliveira Moreira, L. Vinicius de Faria, R. C. Matos, K. B. Enes, M. R. Costa Couri and M. A. L. de Oliveira, Determination of hydroquinone and benzoquinone in pharmaceutical formulations: critical considerations on quantitative analysis of easily oxidized compounds, *Anal. Methods*, 2022, **14**, 4784–4794, DOI: 10.1039/D2AY01631A.

21 X. Deng, X. Chai, C. Wei and L. Fu, Rapid Determination of Quinoline and 2-Hydroxyquinoline in Quinoline Biodegradation Process by Tri-Wavelength UV/Vis Spectroscopy, *Anal. Sci.*, 2011, **27**, 493, DOI: 10.2116/analsci.27.493.

22 M. A. M. Rashid, M. Rahman, A. S. M. O. Mahmud, A. S. M. Morshed, M. M. Haque and M. M. Hossain, *Photochem*, 2022, **2**, 435–447, DOI: 10.3390/photochem2020030.

23 L. Tong, Q. Chen, A. A. Wong, R. Gomez-Bombarelli, A. Aspuru-Guzik, R. G. Gordon and M. J. Aziz, UV-Vis spectrophotometry of quinone flow battery electrolyte for in situ monitoring and improved electrochemical modeling of potential and quinhydrone formation, *Phys. Chem. Chem. Phys.*, 2017, **19**, 31684–31691, DOI: 10.1039/C7CP05881K.

24 H. Meskher and F. Achi, Electrochemical Sensing Systems for the Analysis of Catechol and Hydroquinone in the Aquatic Environments: A Critical Review, *Crit. Rev. Anal. Chem.*, 2024, **54**, 1354–1367, DOI: 10.1080/10408347.2022.2114784.

25 S. Arora, J. Rozon and J. E. Laaser, Dynamics of Ion Locking in Doubly-Polymerized Ionic Liquids, *Macromolecules*, 2021, **54**, 6466–6476, DOI: 10.1021/acs.macromol.0c02637.

26 E. H. Liu, L. W. Qi, J. Cao, P. Li, C. Y. Li and Y. B. Peng, Advances of Modern Chromatographic and Electrophoretic Methods in Separation and Analysis of Flavonoids, *Molecules*, 2008, **13**, 2521–2544, DOI: 10.3390/molecules13102521.

27 U. Anik, S. Timur and Z. Dursun, Metal organic frameworks in electrochemical and optical sensing platforms: a review, *Mikrochim. Acta*, 2019, **186**, 196, DOI: 10.1007/s00604-019-3321-0.

28 A. Rico-Yuste and S. Carrasco, Molecularly Imprinted Polymer-Based Hybrid Materials for the Development of Optical Sensors, *Polymers*, 2019, **11**, 1173, DOI: 10.3390/polym11071173.

29 A. Doron, M. Portnoy, M. Lion-Dagan, E. Katz and I. Willner, Bioelectrocatalyzed Amperometric Transduction of Recorded Optical Signals Using Monolayer-Modified Au-Electrodes, *J. Am. Chem. Soc.*, 1996, **118**, 8937–8944, DOI: 10.1021/ja00129a023.

30 W. Aidli, D. Fumagalli, V. Pifferi and L. Falciola, From dual-mode to multi-modal electrochemical based sensors: A path toward accurate sensing, *Curr. Opin. Electrochem.*, 2025, **50**, 101655, DOI: 10.1016/j.coelec.2025.101655.

31 A. P. Gayatri, N. R. Bandaru, M. G. Bonthu and D. S. Tandu, Advancements and Challenges in Paper-Based Diagnostic Devices for Low-Resource Settings: A Comprehensive Review on Applications, Limitations, and Future Prospects, *Curr. Biotechnol.*, 2025, **14**, 83–107, DOI: 10.2174/0122115501356874250311074358.

32 S. Arora and N. Verma, A review: advancing organic electronics through the lens of ionic liquids and polymerized ionic liquids, *RSC Appl. Polym.*, 2024, **2**, 317–355, DOI: 10.1039/D3LP00269A.

33 J. Liang, K. Xu, S. Arora, J. E. Laaser and S. K. Fullerton-Shirey, Ion-Locking in Solid Polymer Electrolytes for Reconfigurable Gateless Lateral Graphene p–n Junctions, *Materials*, 2020, **13**, 1089, DOI: 10.3390/ma13051089.

34 M. Aslam, K. Ahmad, S. Ali and K. Hamdy, Danishuddin, Recent Progress in Electrocatalysts for Hydroquinone Electrochemical Sensing Application, *Biosensors*, 2025, **15**, 488, DOI: 10.3390/bios15080488.

35 F. Zhao, H. Hu, L. Zhao, H. Yan, H. Zhou, Y. Zhu and Y. Chu, A portable gold microneedle electrochemical sensor for real-time detection of p-benzoquinone in electrolysis process, *Electrochim. Acta*, 2025, **524**, 146050, DOI: 10.1016/j.electacta.2025.146050.

36 T. Xiao, F. Wu, J. Hao, M. Zhang, P. Yu and L. Mao, Ferrocene-mediated enzyme electrode for amperometric determination of glucose, *Anal. Chem.*, 2017, **89**, 300–313, DOI: 10.1021/ac00268a018.

37 S. Arora, J. Liang, S. K. Fullerton-Shirey and J. E. Laaser, A review: advancing organic electronics through the lens of ionic liquids and polymerized ionic liquids, *ACS Mater. Lett.*, 2020, **2**, 331–335, DOI: 10.1039/d3lp00269a.

38 Z. Huo, S. Arora, V. A. Kong, B. J. Myrga, A. Statt and J. E. Laaser, Effect of Polymer Composition and Morphology on Mechanochemical Activation in Nanostructured Triblock Copolymers, *Macromolecules*, 2023, **56**, 1845–1854, DOI: 10.1021/acs.macromol.2c02475.

39 E. Ali, S. Guesmi, H. Essousi, J. Wannassi and H. Barhoumi, Development strategies and applications of cell-based electrochemical taste sensors, *Microchem. J.*, 2025, **215**, 8116–8131, DOI: 10.1007/s11694-025-03551-9.

40 H. Essousi, J. Wannassi, A. Elloumi, E. Ali and H. Barhoumi, Design of Carbon Quantum Dots with Both Yellow/Blue Fluorescence: Enabling Specific Recognition of Oxytetracycline and Tetracycline and Multiscenario, *Microchem. J.*, 2025, **215**, 5789229, DOI: 10.2139/ssrn.5789229.

41 J. Wannassi, M. A. Bouicha, H. Essousi, H. Kahri, H. Nasri, N. Jaffrezic-Renault and H. Barhoumi, Highly Selective and Sensitive Electrochemical Sensor for Mercury(II) Detection Using Nickel(II) (Bromophenyl)porphyrin on a Glassy Carbon Electrode for Environmental Monitoring, *J. Electrochem. Soc.*, 2025, **172**, 047509, DOI: 10.1149/1945-7111/adcbdb.

42 H. Khlifi, H. Wahbi, N. Mhadhbi, F. Saadi, E. Čižmár, A. Sánchez-Coronilla, F. Aouaini, B. Basha, N. B. Hamadi, J. Wannassi, H. Barhoumi and H. Naïli, One-dimensional lead-free copper perovskite: Structural, DFT calculations, thermal stability, magnetic properties, and electrochemical sensing applications, *J. Mol. Struct.*, 2025, **1333**, 141777, DOI: 10.1016/j.molstruc.2025.141777.

43 C. Laberty-Robert, K. Valle, F. Pereira and C. Sanchez, Design and properties of functional hybrid organic–inorganic membranes for fuel cells, *Chem. Soc. Rev.*, 2011, **40**, 961–1005, DOI: 10.1039/C0CS00144A.

44 T. R. Cook, Y. R. Zheng and P. J. Stang, Metal-organic frameworks and self-assembled supramolecular coordination complexes: comparing and contrasting the design, synthesis, and functionality of metal-organic materials, *Chem. Rev.*, 2013, **113**, 734–777, DOI: 10.1021/cr3002824.

45 W. Lu, Z. Wei, Z. Y. Gu, T. F. Liu, J. Park, J. Park, J. Tian, M. Zhang, Q. Zhang, T. Gentle, 3rd, M. Bosch and H. C. Zhou, Tuning the structure and function of metal–organic frameworks *via* linker design, *Chem. Soc. Rev.*, 2014, **43**, 5561–5593, DOI: 10.1039/C4CS00003J.

46 K. Zhou, B. Qi, Z. Liu, X. Wang, Y. Sun and L. Zhang, Nano-Biointeractions of Functional Nanomaterials: The Emerging

Role of Inter-Organelle Contact Sites, Targeting, and Signaling, *Adv. Funct. Mater.*, 2024, **34**, 470306, DOI: 10.1002/adfm.202470306.

47 A. Machin, K. Fontanez, J. C. Arango, D. Ortiz, J. De Leon, S. Pinilla, V. Nicolosi, F. I. Petrescu, C. Morant and F. Marquez, One-Dimensional (1D) Nanostructured Materials for Energy Applications, *Materials*, 2021, **14**, 2609, DOI: 10.3390/ma14102609.

48 B. Su, Y. Wu and L. Jiang, The art of aligning one-dimensional (1D) nanostructures, *Chem. Soc. Rev.*, 2012, **41**, 7832–7856, DOI: 10.1039/C2CS35187K.

49 L. Dou, Y. M. Yang, J. You, Z. Hong, W. H. Chang, G. Li and Y. Yang, Solution-processed hybrid perovskite photodetectors with high detectivity, *Nat. Commun.*, 2014, **5**, 5404, DOI: 10.1038/ncomms6404.

50 I. I. Slowing, B. G. Trewyn, S. Giri and V. S. Y. Lin, Mesoporous Silica Nanoparticles for Drug Delivery and Biosensing Applications, *Adv. Funct. Mater.*, 2007, **17**, 1225–1236, DOI: 10.1002/adfm.200601191.

51 P. G. Bruce, S. A. Freunberger, L. J. Hardwick and J. M. Tarascon, Li-O2 and Li-S batteries with high energy storage, *Nat. Mater.*, 2011, **11**, 19–29, DOI: 10.1038/nmat3191.

52 S.-Y. Lee and S.-J. Park, TiO_2 photocatalyst for water treatment applications, *J. Ind. Eng. Chem.*, 2013, **19**, 1761–1769, DOI: 10.1016/j.jiec.2013.07.012.

53 A. Gaur, A. Singh, A. Kumar, K. S. Kulkarni, S. Lala, K. Kapoor, V. Srivastava, A. Kumar and S. C. Mukhopadhyay, Fire sensing technologies: a review, *IEEE Sens. J.*, 2019, **19**, 3191–3202, DOI: 10.1109/JSEN.2019.2894665.

54 R. K. Joshi and J. J. Schneider, Assembly of one dimensional inorganic nanostructures into functional 2D and 3D architectures. Synthesis, arrangement and functionality, *Chem. Soc. Rev.*, 2021, **41**, 5285–5312, DOI: 10.1039/C2CS35089K.

55 S. V. N. T. Kuchibhatla, A. S. Karakoti, D. Bera and S. Seal, One dimensional nanostructured materials, *Prog. Mater. Sci.*, 2007, **52**, 699–913, DOI: 10.1016/j.pmatsci.2006.08.001.

56 I. Jahan, J. D. Arellano and Z. Shi, Carrier transport mechanisms in polycrystalline semiconductors: from grain boundary physics to device performance, *J. Mater. Chem. C*, 2025, **13**, 23675–23695, DOI: 10.1039/D5TC03750F.

57 Q. Wei, F. Xiong, S. Tan, L. Huang, E. H. Lan, B. Dunn and L. Mai, Porous One-Dimensional Nanomaterials: Design, Fabrication and Applications in Electrochemical Energy Storage, *Adv. Mater.*, 2017, **29**, 1602300, DOI: 10.1002/adma.201602300.

58 A. F. Hiremath, M. R. P. Kumar, K. Rajagopal, R. Barua, S. O. Rab, M. A. Alshehri and T. Bin Emran, Light-regulated RNA interference induced by p-hydroxyphenacyl-modified siRNA in mammalian cells, *Med. Chem.*, 2025, **21**, 772–807, DOI: 10.1080/15257770.2023.2258171.

59 J. Kowalska, J. Rok, Z. Rzepka and D. Wrzesniok, Drug-Induced Photosensitivity-From Light and Chemistry to Biological Reactions and Clinical Symptoms, *Pharmaceuticals*, 2021, **14**, 723, DOI: 10.3390/ph14080723.

60 N. Verma, S. Arora, A. K. Singh and J. Ahmed, Unlocking the potential of exosomes 'extracellular vesicles': drug delivery advancements and therapeutics in ocular diseases, *RSC Pharm.*, 2025, **2**, 1201–1226, DOI: 10.1039/D5PM00097A.

61 A. C. Caires, Recent advances involving palladium (II) complexes for the cancer therapy, *Anti-Cancer Agents Med. Chem.*, 2007, **7**, 484–491, DOI: 10.2174/187152007781668661.

62 S. Arora and C. Mao, Light-regulated RNA interference induced by p hydroxyphenacyl-modified siRNA in mammalian cells, *Nucleosides, Nucleotides Nucleic Acids*, 2024, **43**, 316–339, DOI: 10.1080/15257770.2023.2258171.

63 G. G. Friaza, A. F. Botello, J. M. Pérez, M. J. Prieto and V. Moreno, Synthesis and characterization of palladium(II) and platinum(II) complexes with Schiff bases derivatives of 2-pyridincarboxyaldehyde. Study of their interaction with DNA, *J. Inorg. Biochem.*, 2006, **100**, 1368–1377, DOI: 10.1016/j.jinorgbio.2006.03.011.

64 S. W. Schleser, Q. Krytovych, T. Ziegelmeier, E. Groß, J. Kasparkova, V. Brabec, T. Weber, R. Schobert and T. Mueller, Palladium and Platinum Complexes of the Antimetabolite Fludarabine with Vastly Enhanced Selectivity for Tumour over Non-Malignant Cells, *Molecules*, 2023, **28**, 5173, DOI: 10.3390/molecules28135173.

65 E. Giorgi, F. Binacchi, M. Mannelli, D. Cirri, A. Cesari, M. Boldrini, C. Marotta, C. Ghelarducci, D. Corvaglia, F. Bellina, T. Gamberi, A. Pratesi and C. Gabbiani, Trans-Pd(II) complexes: A different approach for the development of promising anticancer drugs, *Inorg. Chim. Acta*, 2025, **581**, 122645, DOI: 10.1016/j.ica.2025.122645.

66 B. Moulton and M. J. Zaworotko, From Molecules to Crystal Engineering: Supramolecular Isomerism and Polymorphism in Network Solids, *Chem. Rev.*, 2001, **101**, 1629–1658, DOI: 10.1021/cr9900432.

67 M. W. Hosseini, An Approach to the Crystal Engineering of Coordination Networks, Crystal Engineering: From Molecules and Crystals to, *Materials*, 1999, **11**, 181–208, DOI: 10.1007/978-94-011-4505-3_11.

68 I. Uson and G. M. Sheldrick, An introduction to experimental phasing of macromolecules illustrated by SHELX; new autotracing features, *Acta Crystallogr., Sect. D:Struct. Biol.*, 2018, **74**, 106–116, DOI: 10.1107/S2059798317015121.

69 O. V. Dolomanov, L. J. Bourhis, R. J. Gildea, J. A. K. Howard and H. Puschmann, OLEX2: a complete structure solution, refinement and analysis program, *J. Appl. Crystallogr.*, 2009, **42**, 339–341, DOI: 10.1107/S0021889808042726.

70 G. M. Sheldrick, Crystal structure refinement with SHELXL, *Acta Crystallogr., Sect. C:Struct. Chem.*, 2015, **71**, 3–8, DOI: 10.1107/s2053229614024218.

71 D. P. Drolet, D. M. Manuta, A. J. Lees, A. D. Katnani and G. J. Coyle, FT-IR and XPS study of copper(II) complexes of imidazole and benzimidazole, *Inorg. Chim. Acta*, 1988, **146**, 173–180, DOI: 10.1016/S0020-1693(00)80605-2.

72 d. N. D. Marcia Cordes and J. L. Walter, Infrared and Raman spectra of heterocyclic compounds—I the infrared studies and normal vibrations of imidazole, *Spectrochim. Acta, Part A*, 1968, **24**, 237–252, DOI: 10.1016/0584-8539(68)80066-2.

73 B. Morzyk-Ociepa, E. Różycka-Sokołowska and D. Michalska, Revised crystal and molecular structure, FT-IR spectra and DFT studies of chlorotetrakis(imidazole)copper(II) chloride, *J. Mol. Struct.*, 2012, **1028**, 49–56, DOI: 10.1016/j.molstruc.2012.06.028.

74 A. Garcia-Miranda Ferrari, C. W. Foster, P. J. Kelly, D. A. C. Brownson and C. E. Banks, Determination of the Electrochemical Area of Screen-Printed Electrochemical Sensing Platforms, *Biosensors*, 2018, **8**, 53, DOI: 10.3390/bios8020053.

75 Z. Liu, Z. Wang, Y. Cao, Y. Jing and Y. Liu, High sensitive simultaneous determination of hydroquinone and catechol based on graphene/BMIMPF$_6$ nanocomposite modified electrode, *Sens. Actuators, B*, 2011, **157**, 540–546, DOI: 10.1016/j.snb.2011.05.019.

76 H. Yin, Q. Zhang, Y. Zhou, Q. Ma, T. liu, L. Zhu and S. Ai, Electrochemical behavior of catechol, resorcinol and hydroquinone at graphene–chitosan composite film modified glassy carbon electrode and their simultaneous determination in water samples, *Electrochim. Acta*, 2011, **56**, 2748–2753, DOI: 10.1016/j.electacta.2010.12.060.

77 Q. Guo, J. Huang, P. Chen, Y. Liu, H. Hou and T. You, Simultaneous determination of catechol and hydroquinone using electrospun carbon nanofibers modified electrode, *Sens. Actuators, B*, 2012, **163**, 179–185, DOI: 10.1016/j.snb.2012.01.032.

78 B. T. P. Quynh, J. Y. Byun and S. H. Kim, Non-enzymatic amperometric detection of phenol and catechol using nanoporous gold, *Sens. Actuators, B*, 2015, **221**, 191–200, DOI: 10.1016/j.snb.2015.06.067.

79 W. Liu, C. Li, L. Tang, A. Tong, Y. Gu, R. Cai, L. Zhang and Z. Zhang, Nanopore array derived from l-cysteine oxide/gold hybrids: enhanced sensing platform for hydroquinone and catechol determination, *Electrochim. Acta*, 2013, **88**, 15–23, DOI: 10.1016/j.electacta.2012.10.071.

80 L. Zheng, L. Xiong, Y. Li, J. Xu, X. Kang, Z. Zou, S. Yang and J. Xia, Facile preparation of polydopamine-reduced graphene oxide nanocomposite and its electrochemical application in simultaneous determination of hydroquinone and catechol, *Sens. Actuators, B*, 2013, **177**, 344–349, DOI: 10.1016/j.snb.2012.11.006.

81 X. Yuan, D. Yuan, F. Zeng, W. Zou, F. Tzorbatzoglou, P. Tsiakaras and Y. Wang, Preparation and evaluation of nanostructured graphitic carbon material, likely as a catalyst support, *Appl. Catal., B*, 2013, **129**, 367–374, DOI: 10.1016/j.apcatb.2012.09.017.

82 T. Gan, J. Sun, K. Huang, L. Song and Y. Li, A graphene oxide–mesoporous MnO$_2$ nanocomposite modified glassy carbon electrode as a novel and efficient voltammetric sensor for simultaneous determination of hydroquinone and catechol, *Sens. Actuators, B*, 2013, **177**, 412–418, DOI: 10.1016/j.snb.2012.11.033.

83 R. M. A. Tehrani, H. Ghadimi and S. Ab Ghani, Electrochemical studies of two diphenols isomers at graphene nanosheet–poly(4-vinyl pyridine) composite modified electrode, *Sens. Actuators, B*, 2013, **177**, 612–619, DOI: 10.1016/j.snb.2012.11.047.

84 H. S. Han, J.-M. You, H. Seol, H. Jeong and S. Jeon, Electrochemical sensor for hydroquinone and catechol based on electrochemically reduced GO–terthiophene–CNT, *Sens. Actuators, B*, 2014, **194**, 460–469, DOI: 10.1016/j.snb.2014.01.006.

85 CCDC 2482370: Experimental Crystal Structure Determination, 2026, DOI: 10.5517/ccdc.csd.cc2pb3gm.